

See discussions, stats, and author profiles for this publication at: <https://www.researchgate.net/publication/258805869>

# How Gold Nanoparticles Influence Crystallization of Polyethylene in Rigid Cylindrical Nanopores

ARTICLE *in* MACROMOLECULES · JANUARY 2013

Impact Factor: 5.8 · DOI: 10.1021/ma3023876

---

CITATIONS

10

---

READS

98

## 8 AUTHORS, INCLUDING:



[Jon Maiz](#)

Université de Bordeaux/CNRS/Bordeaux INP

13 PUBLICATIONS 239 CITATIONS

[SEE PROFILE](#)



[Gopalakrishnan Trichy Rengarajan](#)

Universität Osnabrück

11 PUBLICATIONS 180 CITATIONS

[SEE PROFILE](#)



[Henning Eickmeier](#)

Universität Osnabrück

86 PUBLICATIONS 352 CITATIONS

[SEE PROFILE](#)



[Martin Steinhart](#)

Universität Osnabrück

181 PUBLICATIONS 5,419 CITATIONS

[SEE PROFILE](#)

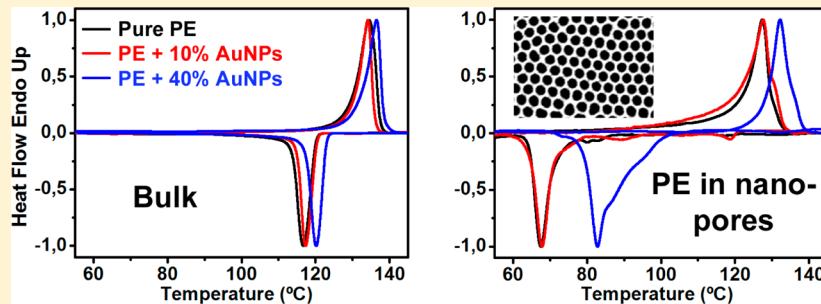
## How Gold Nanoparticles Influence Crystallization of Polyethylene in Rigid Cylindrical Nanopores

Jon Maiz,<sup>†,‡</sup> Helmut Schäfer,<sup>‡</sup> Gopalakrishnan Trichy Rengarajan,<sup>‡</sup> Brigitte Hartmann-Azanza,<sup>‡</sup> Henning Eickmeier,<sup>‡</sup> Markus Haase,<sup>‡</sup> Carmen Mijangos,<sup>†</sup> and Martin Steinhart\*,<sup>‡</sup>

<sup>†</sup>Instituto de Ciencia y Tecnología de Polímeros, CSIC, c/Juan de la Cierva 3, 28006 Madrid, Spain

<sup>‡</sup>Institut für Chemie neuer Materialien, Universität Osnabrück, Barbarastr. 7, D-46069 Osnabrück, Germany

### Supporting Information



**ABSTRACT:** Even high amounts of gold nanoparticles (AuNPs) only moderately influence crystallization of bulk polyethylene (PE). However, under the rigid two-dimensional confinement of aligned cylindrical nanopores in anodic aluminum oxide (AAO) the presence of Au turns nucleation-dominated crystallization of PE at high supercooling into growth-dominated crystallization at lower supercooling. Transmission electron microscopy investigations revealed formation of larger Au crystals from AuNPs by Ostwald ripening. These larger Au crystals apparently acted as heterogeneous nucleation sites initiating PE crystallization in AAO nanopores. Thus, PE/Au composites in AAO exhibited significantly higher crystallization and melting onset temperatures as well as significantly weaker dependence of crystallization half-times on crystallization temperatures. X-ray texture analysis revealed for pure PE in AAO the existence of two copulations of crystals with different orientations (indicative of nucleation-dominated crystal growth); PE/Au composites showed uniform alignment of the fastest growing PE crystal direction with the AAO nanopore axes (indicative of growth-dominated crystallization). The prevailing alignment of the [020] direction of orthorhombic PE with the AAO nanopore axes suggests that properly oriented crystals may form on pre-existing crystal surfaces by secondary nucleation. These secondary crystals grow along the AAO nanopores if, under the conditions of growth-dominated crystallization, competing crystals clogging the growth path are absent while the confinement of the AAO nanopore walls stabilizes the (020) growth faces.

### INTRODUCTION

Crystallization of polymers<sup>1–11</sup> and long-chain alkanes<sup>12</sup> inside cylindrical nanopores or nanotrenches with rigid walls as well as crystallization of crystallizable cylindrical domains in block copolymers<sup>13</sup> has been intensively studied. Crystallization in the two-dimensional confinement of cylindrical nanopores having rigid pore walls is different from bulk crystallization. If crystallization of polymers starts in a bulk reservoir on top of a membrane containing cylindrical nanopores, the crystals forming in the nanopores may have uniform orientation on a macroscopic scale. The crystals are oriented in such a way that the direction of fastest crystal growth, which is typically normal to “rough” crystal faces<sup>14,15</sup> (but not necessarily parallel to the corresponding crystallographic direction), is aligned with the nanopore axes.<sup>2</sup> These findings were rationalized as follows. Owing to the volume of the bulk surface reservoir, which is much larger than that of the polymer in the nanopores, heterogeneous nuclei will predominantly be located in the bulk

surface reservoir. Hence, heterogeneous nucleation<sup>16</sup> in the bulk surface reservoir initiates crystallization at high crystallization temperatures  $T_c$  corresponding to low supercooling. Under these conditions, formation of homogeneous nuclei is, by and large, suppressed. Since the limited number of nuclei at low supercooling results in a likewise small number of growing crystals, crystallization is dominated by crystal growth rather than by nucleation. Crystals having directions of fast growth aligned with the nanopore axes will fill the nanopore volumes, whereas crystals with other orientations impinge on the pore walls. However, the nature of the “gate effect” that leads to exclusive propagation of properly oriented crystals from the bulk surface reservoir into the nanopores has remained elusive.

Received: November 19, 2012

Revised: December 23, 2012

Published: January 10, 2013



Despite the strongly anisotropic confinement imposed by cylindrical nanopores, oriented crystallization can be suppressed if polymeric entities are crystallized while isolated inside the nanopores without being connected with a bulk surface reservoir.<sup>11</sup> Suppression of crystal textures was also reported for cold crystallization following thermal quenching from the melt.<sup>5</sup> Under these conditions, crystallization is initiated at low  $T_c$ s corresponding to high supercooling. At low  $T_c$ s intrinsic nucleation rates are much higher than at low supercooling. Therefore, crystallization is dominated by nucleation. Formation of many nuclei leads to the presence of a high number of growing crystals. Competing crystals are obstacles that confine growth of crystals having directions of fast crystal growth aligned with the nanopore axes. As a result, kinetic domination of crystal orientations allowing fast crystal growth along the nanopores is reduced or even suppressed.

It is obvious that crystallization kinetics significantly impacts orientation, morphology, and the size of polymer crystals formed in cylindrical nanopores and in turn mechanical, optical, electronic, and ferroelectric properties of the crystallized polymeric material. Therefore, manipulation and control of the crystallization of polymers in nanoporous hosts allow adjusting the properties of the resulting nanocomposites. Here, we report the crystallization kinetics of monodisperse linear polyethylene (PE) confined to the cylindrical nanopores of self-ordered anodic aluminum oxide (AAO)<sup>17</sup> in the presence of gold. For this purpose, composites consisting of PE and gold nanoparticles (AuNPs) were infiltrated into AAO. To enhance compatibility of the AuNPs with PE, the AuNPs were modified with dodecanethiol. PE can be considered as “prototypical chain polymer”,<sup>18</sup> the crystallization of which was extensively studied in bulk systems,<sup>18–20</sup> in block copolymers<sup>21–23</sup> and inside AAO.<sup>4,9</sup> Moreover, agglomerated NPs in bulk PE nanocomposites have been reported to induce nucleation.<sup>24–28</sup>

As discussed below, the presence of Au influences crystallization of PE under the rigid cylindrical confinement imposed by the AAO nanopore walls much stronger than in bulk systems. In AAO, a significant shift to heterogeneous nucleation and growth-dominated crystallization at low supercooling is observed.

## EXPERIMENTAL SECTION

**Synthesis of Thiol-Derivatized AuNPs.** Colloidal AuNPs were synthesized according to procedures reported previously.<sup>29–31</sup> An aqueous solution of hydrogen tetrachloroaurate (30 mL, 30 mmol/dm) was mixed with a solution of tetraoctylammonium bromide in toluene (80 mL, 50 mmol/dm). The two-phase mixture was vigorously stirred until all the tetrachloroaurate was transferred into the organic phase. Then, 170 mg of dodecanethiol was added and dissolved in the organic phase. Finally, a freshly prepared aqueous solution of sodium borohydride (25 mL, 0.4 mol/dm) was slowly added under vigorous stirring. After further stirring for 3 h, the organic phase was separated, evaporated to 10 mL in a rotary evaporator, and mixed with 400 mL of ethanol to remove excess dodecanethiol. The mixture was kept for 4 h at –18 °C. Then, the dark brown precipitate was filtered off and washed with ethanol. The crude product was dissolved in 10 mL of toluene and again precipitated with 400 mL of ethanol. The dodecanethiol-capped AuNPs thus obtained were dissolved in toluene. The overall concentration of the resulting AuNP solution was estimated 1.5 wt %. As-prepared AuNPs had diameters ranging from 2 to 7 nm (Figure S1a,b). The size distribution of the AuNPs in an aliquot (2–3 mL) of the suspension in toluene was studied by dynamic light scattering (DLS) using a Nanosizer (Malvern Instruments, Malvern UK). The maximum of the particle size distribution, as determined by DLS, was around 3.5 nm (Figure S1c).

**Self-Ordered AAO.** Self-ordered AAO contains arrays of aligned cylindrical nanopores with narrow diameter distribution. The AAO nanopores are straight, uniform in depth, and not interconnected. Self-ordered AAO was prepared by the two-step anodization introduced by Masuda and co-workers.<sup>17</sup> Ultrapure aluminum disks (diameter 2 cm, thickness 500 μm, purity >99.999%, supplier: Goodfellow) were anodized at 40 V and 3–5 °C using 0.3 M oxalic acid as electrolyte solution. The pores were widened to 60 nm by isotropic etching with 5 wt % phosphoric acid at 30 °C. All self-ordered AAO membranes used in this work had a nanopore diameter of 60 nm and a pore depth of 100 μm.

**PE and PE\_Au Nanocomposites.** PE ( $M_w = 36\,500$  g/mol,  $M_w/M_n = 1.31$ ; purchased from Polymer Standards Service) was used as received. To prepare composite films of PE and AuNPs, 1.5 wt % suspensions of dodecanethiol-capped AuNPs in toluene were mixed with 10 wt % solutions of PE in toluene. The mixtures were vigorously stirred for 1 day and cast onto glass slides. Subsequently, the solvent was slowly evaporated in air at room temperature. The prepared PE films contained either ~10 wt % Au (PE\_Au\_10%) or ~40 wt % Au (PE\_Au\_40%). The content of pure Au in bulk PE\_Au\_10% was determined by thermogravimetric analysis (TGA) using a TGA unit Netzsch STA 449 C (Figure S2). We calculated the mixing ratio of the PE solution and the AuNP suspension for PE\_Au\_40% based on the thermogravimetric analysis of PE\_Au\_10%.

**Transmission Electron Microscopy (TEM).** PE\_Au\_10% and PE\_Au\_40% were crystallized in AAO without bulk surface reservoir applying the same procedures as in case of the samples used for wide-angle X-ray scattering (see below). Infiltration into AAO at 180 °C for 60 min was followed by cooling to room temperature at a rate of –1 K/min in the presence of a bulk surface reservoir. Then, the bulk surface reservoirs were scraped off with sharp blades. The samples were again heated to 180 °C for 10 min and cooled to room temperature at a rate of –1 K/min. All high-temperature steps were carried out in an argon atmosphere or under vacuum. We etched the aluminum substrate to which the AAO was connected with a mixture of 3.4 g of CuCl<sub>2</sub>·2H<sub>2</sub>O, 100 mL of H<sub>2</sub>O, and 100 mL of concentrated HCl<sub>(aq)</sub>. Subsequently, the AAO was etched using an aqueous 5 wt % KOH solution. The KOH solution containing the released PE\_Au\_40% nanorods was dropped onto copper grids coated with carbon films. After evaporation of the water, the precipitated KOH was removed by several washing steps including deposition of a drop of deionized water on the copper grid followed by its careful removal with a syringe. TEM measurements were conducted on a JEOL JEM-2100 microscope operated at 200 kV.

**Differential Scanning Calorimetry (DSC).** Pure PE, PE\_Au\_10%, and PE\_Au\_40% were melt-infiltrated into self-ordered AAO heated to 180 °C for 60 min under argon or vacuum. The bulk surface reservoirs were scraped off and the aluminum substrates of the AAO membranes were removed as described above. All measurements were carried out using a DSC PerkinElmer 8500 equipped with an Intracooler 3 cooling unit. DSC traces of infiltrated AAO samples were recorded with reference pans containing empty AAO pieces of the same size. Nonisothermal measurements were conducted at heating and cooling rates of ±10 K/min. For isothermal crystallization experiments, the samples were heated above their melting temperatures  $T_m$  for 10 min. Then, the samples were quenched to a selected isothermal crystallization temperature  $T_c$  and kept at  $T_c$  for selected crystallization times  $t$ . Subsequent heating runs taken at a heating rate of +10 K/min yielded melting endotherms representative of the isothermal crystallization process.

**Wide-Angle X-ray Scattering (WAXS).** Pure PE, PE\_Au\_10%, and PE\_Au\_40% were melt-infiltrated into self-ordered AAO at 180 °C for 60 min and nonisothermally crystallized at a cooling rate of –1 K/min while connected with a bulk reservoir on the AAO surface. Then, the bulk surface reservoirs were scraped off using sharp blades. One set of samples was directly studied by WAXS (X-ray patterns represent crystallization with bulk surface reservoir). Another set of samples was again heated to 180 °C for 10 min and crystallized at a cooling rate of –1 K/min without bulk surface reservoir (WAXS patterns represent crystallization of PE entities isolated in the AAO

nanopores). All high-temperature steps were carried out in argon or under vacuum. WAXS measurements in reflection were performed using a PANalytical X'Pert Pro MRD diffractometer operated with Cu K $\alpha$  radiation. During  $\Theta/2\Theta$  scans, the AAO surface was oriented perpendicular to the scattering plane defined by incident beam and detector, and  $\Theta$  was the angle enclosed by incident beam and AAO surface (Figure S3). In this geometry, only crystals that meet the Bragg condition and that have the corresponding set of lattice planes oriented parallel to the AAO surface (normal to the AAO nanopore axes) contribute to the detected scattering intensity  $I(\Theta)$ .<sup>11</sup> Coherence lengths  $D_{020}$  along the [020] direction of orthorhombic PE in AAO (in orthorhombic systems the [020] direction is perpendicular to the (020) planes) were estimated by the Scherrer method<sup>32</sup> according to

$$D_{020} = \frac{K\lambda}{\Delta(2\Theta) \cos \Theta} \quad (1)$$

where  $\lambda = 0.154$  nm is the wavelength of the X-rays,  $\Theta$  the scattering angle,  $\Delta(2\Theta)$  the full width at half-maximum of the evaluated reflection in radians, and  $K = 0.89$  the dimensionless Scherrer form factor. The obtained  $D_{020}$  values can be considered as lower limits of the actual coherence lengths along the [020] direction.

Orientation distributions with respect to the AAO surface of sets of lattice planes belonging to specific reflections were determined by Schulz scans.<sup>33,34</sup> In the course of a Schulz scan, the  $\Theta$  and  $2\Theta$  angles are fixed. The AAO is tilted about the  $\Psi$  axis by a tilt angle  $\Psi$  (note that the angle  $\Psi$  is denoted  $\phi$  in ref 4). The  $\Psi$  axis lies in the scattering plane as well as in the plane of the AAO surface and is oriented perpendicular to the  $\Theta/2\Theta$  axis as well as to the AAO nanopore axes (Figure S3). As a result, Schulz scans yield intensity profiles  $I(\Psi)$  that correspond to azimuthal intensity profiles along the Debye rings belonging to the fixed scattering angles  $\Theta$ .  $I(\Psi)$  is only accessible up to  $\Psi \approx 70^\circ$  because of defocusing effects.<sup>35</sup> The Hermans order parameter  $f^3$ <sup>6</sup> is a frequently used measure for the degree of orientation relative to a reference direction in uniaxial systems. An  $f$  value of 1 indicates perfect uniaxial orientation, whereas an  $f$  value of zero indicates the absence of any nonrandom orientation. Hermans order parameters of the orientation distributions of (020) lattice planes relative to the AAO surface were calculated from baseline-corrected  $I(\Psi)$  profiles obtained by Schulz scans according to

$$f = \frac{3}{2} \langle \cos^2 \Psi \rangle - \frac{1}{2} \quad (2)$$

where for a Schulz scan yielding  $h$  values of  $I(\Psi)$

$$\langle \cos^2 \Psi \rangle = \frac{\sum_{i=1}^h [I(\Psi)_i \cos^2 \Psi_i]}{\sum_{i=1}^h I(\Psi)_i} \quad (3)$$

## RESULTS

**Morphology.** Figure 1 shows TEM images of released PE\_Au\_40% nanorods that had lengths of at least several tens of micrometers, whereas their diameter of  $\sim 60$  nm corresponded to the diameter of the AAO nanopores. Figure 1a shows a large-field TEM image of a fabric of PE\_Au\_40% nanorods containing Au crystals having sizes of a few tens of nanometers. Occasionally, even cylindrical Au crystals that apparently grew along AAO nanopores were found; for example, a cylindrical Au crystal with a diameter of  $\sim 50$  nm and a length of  $\sim 200$  nm is seen in Figure 1b. Apparently, Ostwald ripening<sup>37</sup> resulted in the formation of Au crystals that are significantly larger than the as-synthesized AuNPs. This observation is in line with previous results on the thermolysis of tetrachloroaurate in AAO, yielding long single-crystalline Au nanorods.<sup>38</sup> A significant portion of the PE\_Au\_40% nanorod segments showed surface undulations (Figure 1c). Released PE\_Au\_10% nanorods contained only very occasionally single

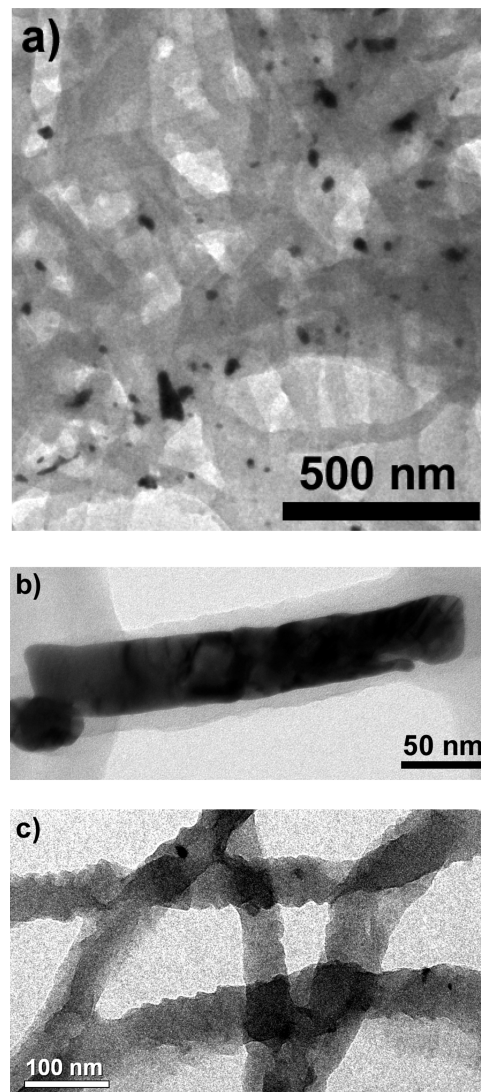


**Figure 1.** TEM images of released PE\_Au\_40% nanorods non-isothermally crystallized without bulk surface reservoir at a rate of  $-1$  K/min. (a) Large-field view of a fabric of PE\_Au\_40% nanorods. The dark spots are Au crystals. (b) Detail showing a pluglike Au crystal grown along an AAO nanopore. (c) PE\_Au\_40% nanorods with undulated surface.

AuNPs (Figure 2). Moreover, we could not find PE\_Au\_10% nanorods exhibiting surface undulations.

**Nonisothermal Crystallization: Kinetics.** DSC cooling runs reflecting nonisothermal crystallization and subsequently measured second heating runs of bulk PE, bulk PE\_Au\_10% and bulk PE\_Au\_40% as well as of PE in AAO, PE\_Au\_10% in

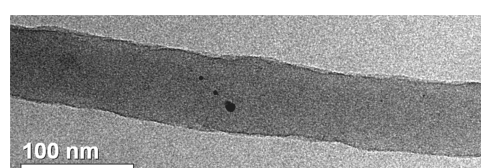


**Figure 2.** TEM image of a released PE\_Au\_10% nanorod non-isothermally crystallized without bulk surface reservoir at a rate of  $-1$  K/min. The dark spots are dispersed AuNPs occasionally found in PE\_Au\_10% nanorods.

AAO, and PE\_Au\_40% in AAO are shown in Figure 3. The corresponding crystallization onset temperatures  $T_{c,\text{onset}}$ , the

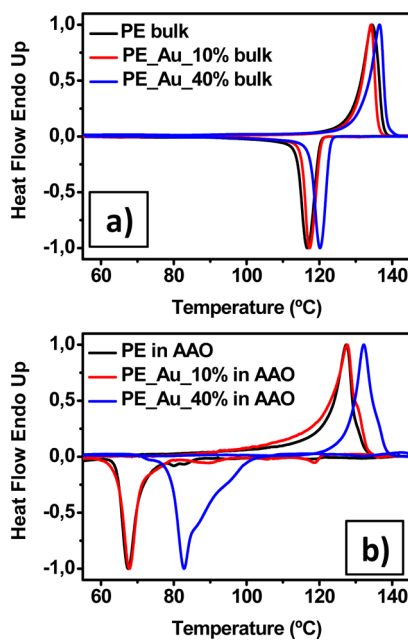


**Figure 3.** Investigation of nonisothermal crystallization kinetics of PE, PE\_Au\_10%, and PE\_Au\_40% by DSC (cooling and heating rates: 10 K/min). (a) Cooling runs and subsequently measured second heating runs of bulk PE, bulk PE\_Au\_10%, and bulk PE\_Au\_40%. (b) Cooling runs and subsequently measured second heating runs of PE, PE\_Au\_10%, and PE\_Au\_40% inside AAO.

temperatures of the crystallization peak maxima  $T_{c,\text{peak}}$ , the melting onset temperatures  $T_{m,\text{onset}}$ , and the temperatures of the melting peak maxima  $T_{m,\text{peak}}$  are listed in Table 1. Non-

**Table 1. Results of DSC Scans (Cooling and Heating Rates: 10 K/min): Onset Temperatures of the Melting Endotherms  $T_{m,\text{onset}}$ , Temperatures of the Maxima of the Melting Endotherms  $T_{m,\text{peak}}$ , Onset Temperatures of the Crystallization Exotherms  $T_{c,\text{onset}}$ , and Temperatures of the Maxima of the Crystallization Exotherms  $T_{c,\text{peak}}$**

|                  | $T_{m,\text{onset}}$ (°C) | $T_{m,\text{peak}}$ (°C) | $T_{c,\text{onset}}$ (°C) | $T_{c,\text{peak}}$ (°C) |
|------------------|---------------------------|--------------------------|---------------------------|--------------------------|
| bulk PE          | 129                       | 135                      | 120                       | 117                      |
| bulk PE_Au_10%   | 130                       | 134                      | 120                       | 117                      |
| bulk PE_Au_40%   | 132                       | 137                      | 123                       | 120                      |
| PE in AAO        | 122                       | 127                      | 77                        | 67                       |
| PE_Au_10% in AAO | 121                       | 128                      | 78                        | 68                       |
| PE_Au_40% in AAO | 128                       | 132                      | 99                        | 83                       |

isothermal crystallization of bulk PE is typically initiated by heterogeneous nucleation; as expected, in bulk PE crystal growth occurred just below the melting temperature range within a relatively narrow temperature window. Bulk Au\_PE\_10% showed the same crystallization kinetics and melting behavior than bulk PE. As compared to bulk PE and bulk PE\_Au\_10%, both melting and crystallization of bulk PE\_Au\_40% were shifted to slightly higher temperatures.

Crystallization of PE inside the AAO nanopores occurred, in general, at lower temperatures as in the corresponding bulk samples (during the DSC experiments, the PE in the AAO nanopores was isolated; nucleation had to take place separately

in each crystallizing AAO nanopore). In the DSC heating and cooling scans, pure PE in AAO and PE\_Au\_10% in AAO showed, by and large, the same behavior. Strikingly,  $T_{c,\text{onset}}$  of PE\_Au\_40% in AAO was ~20 K above  $T_{c,\text{onset}}$  of pure PE in AAO and PE\_Au\_10% in AAO.  $T_{c,\text{peak}}$  of PE\_Au\_40% in AAO was ~15 K above  $T_{c,\text{peak}}$  of pure PE in AAO and PE\_Au\_10% in AAO. Moreover,  $T_{m,\text{onset}}$  of PE\_Au\_40% in AAO was ~6 K higher than  $T_{m,\text{onset}}$  of pure PE in AAO and of PE\_Au\_10% in AAO. Finally,  $T_{m,\text{peak}}$  of PE\_Au\_40% in AAO was 4 K higher than  $T_{m,\text{peak}}$  of PE and PE\_Au\_10% in AAO.

**Nonisothermal Crystallization: Crystal Textures.** Characteristic reflections of orthorhombic PE are the (110) reflection at  $2\Theta = 21.4^\circ$ , the (200) reflection at  $2\Theta = 24.0^\circ$ , and the (020) reflection at  $2\Theta = 36.3^\circ$ .<sup>39,40</sup> The (110) and (200) reflections of bulk PE have relative intensities of 100% and 37%, respectively, whereas the relatively weak (020) reflection has a relative intensity of only 4% (Figure 4a). The

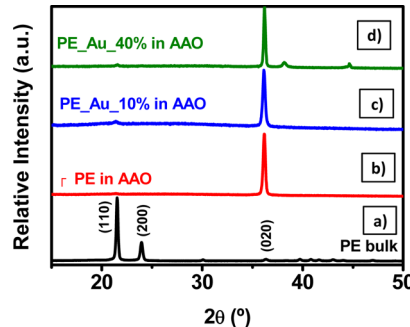


**Figure 4.**  $\Theta/2\Theta$  scans of PE, PE\_Au\_10%, and PE\_Au\_40% inside AAO crystallized in the presence of bulk reservoirs on the AAO surface (surface reservoirs were removed prior to XRD measurements). (a) Bulk PE having the same thermal history shown for comparison. (b) PE inside AAO. (c) PE\_Au\_10% inside AAO. (d) PE\_Au\_40% inside AAO. In panel d, the (110) peak of Au at  $2\Theta = 38.2^\circ$  and the (200) peak of Au at  $2\Theta = 44.6^\circ$  can be seen.

crystal textures of PE in AAO, PE\_Au\_10% in AAO, and PE\_Au\_40% in AAO nonisothermally crystallized at a cooling rate of -1 K/min were studied by  $\Theta/2\Theta$  scans. Moreover, orientation distributions of sets of lattice planes belonging to the above-mentioned characteristic reflections of orthorhombic PE relative to the AAO surface were obtained by Schulz scans. Figure 4 shows  $\Theta/2\Theta$  scans of PE, PE\_Au\_10%, and PE\_Au\_40% in AAO crystallized while connected with a bulk surface reservoir (which was removed before the measurements). In all cases, only a very intense (020) reflection appears. The coherence lengths along the [020] direction parallel to the AAO nanopore axes estimated by the Scherrer method<sup>32</sup> amounted to ~31 nm for pure PE in AAO, to ~28 nm for PE\_Au\_10% in AAO, and to ~38 nm for PE\_Au\_40%. The coherence length along the [020] direction in the bulk reference sample (also crystallized at a cooling rate of -1 K/min) amounted to only ~20 nm. In the diffraction pattern of PE\_Au\_40% in AAO also the (110) reflection of Au at  $2\Theta = 38.2^\circ$  and the (200) reflection of Au at  $2\Theta = 44.6^\circ$  can be seen (Figure 4d). The (020) lattice planes of PE, PE\_Au\_10%, and PE\_Au\_40% in AAO crystallized with bulk surface reservoirs had narrow orientation distributions with respect to the AAO surface. This is obvious from the narrow  $I(\Psi)$  peaks centering about  $\Psi = 0^\circ$  in the corresponding Schulz scans (Figure 5). The half-widths at half-maximum (hwhm) of the corresponding

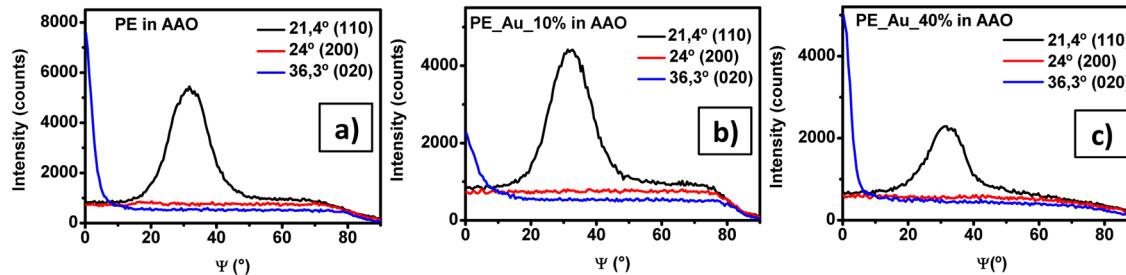


**Figure 5.** Schulz scans of PE, PE\_Au\_10%, and PE\_Au\_40% nanorods inside AAO crystallized in contact with a bulk surface reservoir (surface reservoirs were removed prior to XRD measurements). The black lines are Schulz scans of the (110) reflection, the red lines of the (200) reflections, and the blue lines of the (020) reflections. (a) PE inside AAO. (b) PE\_Au\_10% inside AAO. (c) PE\_Au\_40% inside AAO.

$I(\Psi)$  peaks amounted to  $\sim 2.3^\circ$  for pure PE in AAO, to  $3.7^\circ$  for PE\_Au\_10% in AAO, and to  $\sim 2.7^\circ$  for PE\_Au\_40% in AAO; the Hermans order parameters  $f$  ranged from 0.97 to 0.98. The Schulz scans belonging to the (110) reflections exhibited only single peaks at  $\Psi \approx 33^\circ$ , corresponding to the angle between the (020) and (110) lattice planes. No  $I(\Psi)$  maximum within the covered  $\Psi$  range is apparent for the (200) reflection—the angle between the (020) and (200) lattice planes is  $90^\circ$  so that the  $I(\Psi)$  maximum of the (200) reflection would occur outside the accessible  $\Psi$  range at  $\Psi = 90^\circ$ .

Subsequent crystallization of PE, PE\_Au\_10%, and PE\_Au\_40% in AAO without bulk surface reservoir resulted again in dominance of crystals having their (020) lattice planes oriented normal to the AAO nanopore axes. The (110) and (200) reflections are weaker than expected for isotropic distributions of crystal orientations, whereas the (020) reflections are very intensive (Figure 6). However, in contrast

nanopore axes, pure PE in AAO crystallized without bulk surface reservoir had a coherence length of  $\sim 23$  nm, PE\_Au\_10% of  $\sim 28$  nm, and PE\_Au\_40% of  $\sim 34$  nm. Schulz scans belonging to the (020) reflection of PE, PE\_Au\_10%, and PE\_Au\_40% crystallized in AAO without bulk surface reservoir (Figure 7) show a peak at  $\Psi \approx 0^\circ$  that is weak in the case of PE ( $f = 0.95$ , hwhm =  $5.8^\circ$ ), more pronounced in the case of PE\_Au\_10% ( $f = 0.98$ , hwhm =  $4.2^\circ$ ), and most pronounced in the case of PE\_Au\_40% ( $f = 0.99$ , hwhm =  $2.7^\circ$ ). As in the case of the samples crystallized with bulk surface reservoir, no peak is apparent in the  $I(\Psi)$  profiles belonging to the (200) reflection. The  $I(\Psi)$  profiles belonging to the (110) reflection of PE and PE\_Au\_10 crystallized in AAO without bulk surface reservoir show a bimodal orientation distribution of the (110) lattice planes with two pronounced maxima at  $\Psi \approx 33^\circ$  and  $\Psi \approx 66^\circ$ . However, the  $I(\Psi)$  profile of the (110) reflection of PE\_Au\_40 crystallized in AAO without bulk surface reservoir shows only one maximum at  $\Psi \approx 33^\circ$ . Hence, it resembles the  $I(\Psi)$  profiles of the (110) reflections of PE\_Au\_40 crystallized in AAO in the presence of a bulk surface reservoir.

**Kinetics of Isothermal Crystallization.** DSC traces representing isothermal crystallization of bulk PE, bulk PE\_Au\_10%, and bulk PE\_Au\_40% as well as isothermal crystallization without bulk surface reservoir of PE in AAO, PE\_Au\_10% in AAO, and PE\_Au\_40% in AAO are shown in Figure S4. The values of the Avrami exponent  $n$  (Figure 8a) were determined from the slopes of the corresponding Avrami plots<sup>41</sup> (Supporting Information, text 1 and Figure S5). The  $n$  values of bulk PE lay between 2.2 and 3.1, whereas the  $n$  values of PE in AAO, PE\_Au\_10% in AAO, and PE\_Au\_40% in AAO ranged from 1.3 to 2.1. The dependencies of the crystallization half times  $t_{1/2}$  and the reciprocal crystallization half-times  $t_{1/2}^{-1}$  on  $T_c$  (Figure 8b–d) are summarized in Table 2. In contrast to bulk PE\_Au\_40%, the presence of Au significantly affected crystallization kinetics of PE\_Au\_40% in AAO. Strikingly, the slope  $d(t_{1/2}^{-1})/dT_c$  of PE\_Au\_40% in AAO is 1 order of magnitude smaller than the slopes  $d(t_{1/2}^{-1})/dT_c$  of PE in AAO and of PE\_Au\_10% in AAO.

The same trends were observed for the melting of PE after isothermal crystallization (Figure 9).  $T_{m,\text{onset}}$  of the bulk samples ranged from 131 to 135 °C and  $T_{m,\text{peak}}$  from 137 to 140 °C.  $T_{m,\text{onset}}$  and  $T_{m,\text{peak}}$  showed a weak dependence on  $T_c$ , but no systematic differences between the different samples were apparent.  $T_{m,\text{onset}}$  and  $T_{m,\text{peak}}$  of bulk PE\_Au\_40 were equal to or even smaller than  $T_{m,\text{onset}}$  and  $T_{m,\text{peak}}$  of bulk PE and bulk PE\_Au\_10%.  $T_{m,\text{onset}}$  and  $T_{m,\text{peak}}$  of PE in AAO, PE\_Au\_10% in AAO, and PE\_Au\_40% in AAO were practically independent of  $T_c$ .  $T_{m,\text{onset}}$  of PE in AAO and

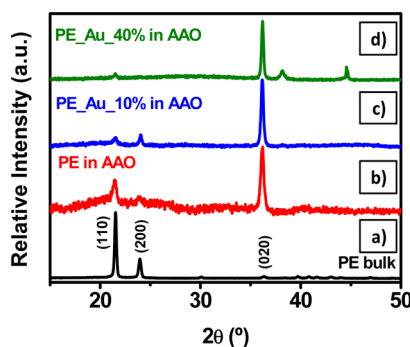


**Figure 6.**  $\Theta/2\Theta$  scans of PE, PE\_Au\_10%, and PE\_Au\_40% crystallized in the separated state inside AAO nanopores (surface reservoirs were removed before crystallization). (a) Bulk PE having the same thermal history shown for comparison. (b) PE inside AAO. (c) PE\_Au\_10% inside AAO. (d) PE\_Au\_40% inside AAO. In panel d, the (110) peak of Au at  $2\Theta = 38.2^\circ$  and the (200) peak of Au at  $2\Theta = 44.6^\circ$  can be seen.

to the samples crystallized in the presence of a bulk surface reservoir, the (110) reflection is clearly present in all patterns and the (200) reflection appears in the patterns of PE in AAO and PE\_Au\_10% in AAO. The ratios of the relative intensities of the (110), (200), and (020) peaks amount to 0.39:0.15:1 for PE in AAO and to 0.13:0.18:1 for PE\_Au\_10% in AAO. In the case of PE\_Au\_40% in AAO, the ratio of the relative intensities of the (110) and (020) peaks is 0.07:1. Moreover, the (110) peak of Au at  $2\Theta = 38.2^\circ$  and the (200) peak of Au at  $2\Theta = 44.6^\circ$  can be seen in the pattern of PE\_Au\_40% in AAO (Figure 6d). Along the [020] direction parallel to the AAO

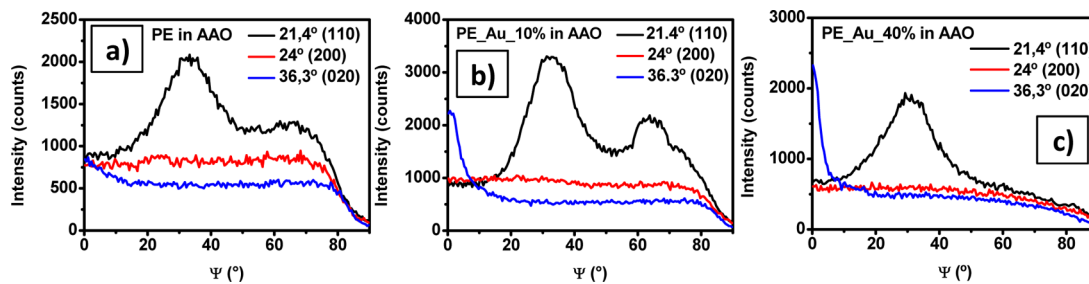


**Figure 7.** Schulz scans of PE, PE\_Au\_10%, and PE\_Au\_40% inside AAO crystallized without bulk surface reservoir. The black lines are Schulz scans of the (110) reflection, the red lines of the (200) reflection, and the blue lines of the (020) reflection. (a) PE inside AAO. (b) PE\_Au\_10% inside AAO. (c) PE\_Au\_40% inside AAO.

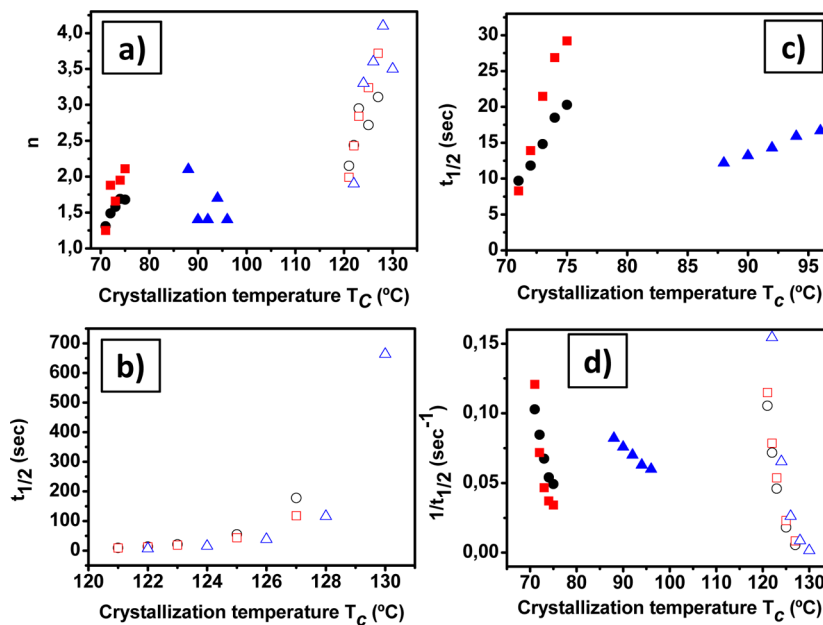


**Figure 8.** (a) Avrami exponent  $n$  as a function of isothermal crystallization temperature  $T_c$ . (b) Crystallization half-times  $t_{1/2}$  of bulk PE, bulk PE\_Au\_10%, and bulk PE\_Au\_40% as a function of isothermal crystallization temperature  $T_c$ . (c) Crystallization half-times  $t_{1/2}$  of PE in AAO, PE\_Au\_10% in AAO, and PE\_Au\_40% in AAO as a function of isothermal crystallization temperature  $T_c$ . (d) Crystallization rate  $1/t_{1/2}$  as a function of isothermal crystallization temperature  $T_c$ . Symbols: ○, bulk PE; □, bulk PE\_Au\_10%; △, bulk PE\_Au\_40%; ●, PE in AAO; ■, PE\_Au\_10% in AAO; ▲, PE\_Au\_40% in AAO.

**Table 2. Slopes  $d(t_{1/2})/dT_c$  of the Crystallization Half-Times  $t_{1/2}$  and Slopes  $d(t_{1/2}^{-1})/dT_c$  of the Reciprocal Crystallization Half-Times  $t_{1/2}^{-1}$  as a Function of the Isothermal Crystallization Temperature  $T_c$  Obtained from Linear Fits of the Data Displayed in Figure 8**

| sample           | $d(t_{1/2})/dT_c$ ( $s K^{-1}$ ) | $d(t_{1/2}^{-1})/dT_c$ ( $s^{-1} K^{-1}$ ) |
|------------------|----------------------------------|--|
| bulk PE          |                                  | $1.6 \times 10^{-2}$                       |
| bulk PE_Au_10%   |                                  | $1.7 \times 10^{-2}$                       |
| bulk PE_Au_40%   |                                  | $1.8 \times 10^{-2}$                       |
| PE in AAO        | 2.79                             | $1.4 \times 10^{-2}$                       |
| PE_Au_10% in AAO | 5.49                             | $2.1 \times 10^{-2}$                       |
| PE_Au_40% in AAO | 0.59                             | $2.9 \times 10^{-3}$                       |

PE\_Au\_10% in AAO lay in the range from 124 to 125 °C and  $T_{m,\text{peak}}$  in the range from 130 to 131 °C. However, in the case of PE\_Au\_40% in AAO both temperatures were systematically shifted to higher values:  $T_{m,\text{onset}}$  of PE\_Au\_40% in AAO amounted to ~129 °C and  $T_{m,\text{peak}}$  to ~132 °C.

## DISCUSSION

**Impact of Au on Crystallization Kinetics of PE in AAO.** Bulk PE and bulk PE\_Au\_10% showed identical behavior during nonisothermal and isothermal crystallization. This finding is not unexpected—it is well-known that small amounts of dispersed inorganic NPs do not influence nucleation and may even act as obstacles for crystallization.<sup>24,28</sup> However, higher contents of inorganic NPs in PE nanocomposites were reported to enhance heterogeneous nucleation to some extent. Consistent with our results summarized above, Avrami exponents  $n$  for such nanocomposites typically range from 1.7 to 2.0 and were interpreted as a signature of heterogeneous nucleation combined with confined crystal growth.<sup>24–27</sup> In agreement with these reports, bulk PE\_Au\_40% showed a slight shift to higher crystallization and melting temperatures as compared to bulk PE and bulk PE\_Au\_10% in nonisothermal crystallization experiments (Table 1). However, no significant differences between bulk PE, bulk PE\_Au\_10%, and bulk PE\_Au\_40% were apparent in isothermal crystallization experiments.

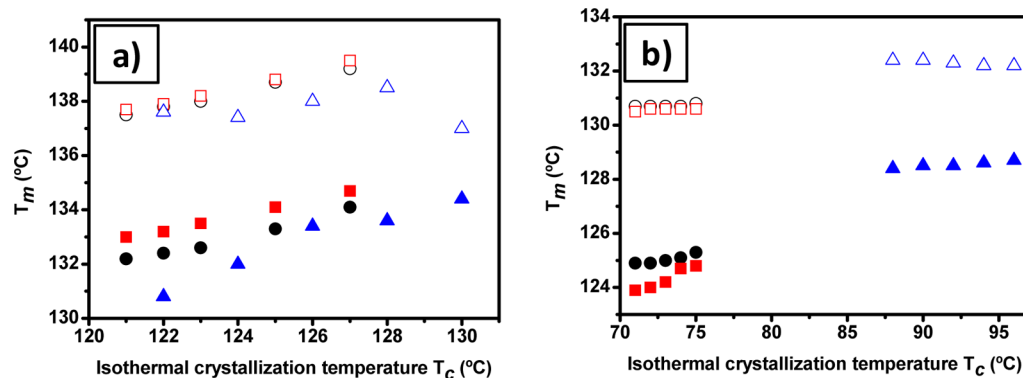


**Figure 9.** Onset temperatures of the melting endotherms  $T_{m,\text{onset}}$  (solid symbols) and temperatures at the maxima of the melting endotherms  $T_{m,\text{peak}}$  (open symbols) plotted against the isothermal crystallization temperature  $T_c$ . (a) Bulk PE (●, ○), bulk PE\_Au 10% (■, □), and bulk PE\_Au 40% (▲, △). (b) PE in AAO (●, ○), PE\_Au\_10% in AAO (■, □), and PE\_Au\_40% in AAO (▲, △).

Crystallization of pure PE in AAO essentially reproduced the results previously obtained by Shin and co-workers using AAO with a similar nanopore diameter.<sup>4,9</sup> As in the bulk, pure PE in AAO and PE\_Au\_10% in AAO showed largely the same behavior in both nonisothermal and isothermal crystallization experiments, indicating that the presence of small amounts of AuNPs does not significantly influence crystallization of PE in AAO. However, the differences in crystallization behavior between PE in AAO as well as PE\_Au\_10% in AAO, on the one hand, and PE\_Au\_40% in AAO, on the other, are striking, all the more as such differences were not apparent for the corresponding bulk materials. The modified crystallization behavior of PE\_Au\_40% in AAO can be summarized as follows:

- (1) During cooling from the melt, nonisothermal crystallization of PE\_Au\_40% in AAO starts at significantly higher  $T_{c,\text{onset}}$  values than nonisothermal crystallization of PE in AAO and PE\_Au\_10% in AAO. In general, PE\_Au\_40% in AAO crystallizes at significantly higher temperatures than PE in AAO and PE\_Au\_10% in AAO.
- (2) Isothermal crystallization kinetics of PE\_Au\_40% in AAO significantly differs from isothermal crystallization kinetics of PE in AAO and PE\_Au\_10% in AAO. The dependencies of  $t_{1/2}$  and  $t_{1/2}^{-1}$  on  $T_c$  are much weaker for PE\_Au\_40% in AAO, and the slopes  $d(t_{1/2})/dT_c$  (Figure 8c) as well as  $d(t_{1/2}^{-1})/dT_c$  (Figure 8d) are much smaller. A similar transition to smaller slopes  $d(t_{1/2}^{-1})/dT_c$  was reported by Woo et al. when the AAO nanopore diameter was reduced from 62 to 48 nm.<sup>9</sup> These authors interpreted this observation as a crossover from predominantly homogeneous nucleation in larger AAO nanopores, resulting in strong dependence of the crystallization rates on  $T_c$ , to heterogeneous nucleation at the nanopore walls in the smaller AAO nanopores, resulting in weaker dependence of the crystallization rates on  $T_c$ .
- (3) The presence of AuNPs does not significantly alter melting of bulk PE, bulk PE\_Au\_10%, and bulk PE\_Au\_40%. However,  $T_{m,\text{onset}}$  of nonisothermally as well as of isothermally crystallized PE\_Au\_40% in AAO is significantly higher than  $T_{m,\text{onset}}$  of PE in AAO and PE\_Au\_10% in AAO (Figures 3 and 9, Table 1). This outcome suggests that PE in AAO and PE\_Au\_10% in AAO contain a certain fraction of small PE crystals formed at low  $T_c$ , whereas PE\_Au\_40% in AAO does not

contain such small crystals as crystallization takes place at a higher  $T_c$ . We speculate that not only lamella thickness but also lateral lamella interfaces influence the melting point of these small crystals. The [020] coherence lengths along the AAO nanopores estimated for nonisothermally crystallized PE in AAO, PE\_Au\_10% in AAO, and PE\_Au\_40% in AAO from the  $\Theta/2\Theta$  scans shown in Figures 4 and 6 are consistent with this interpretation. Moreover,  $T_{m,\text{peak}}$  of PE\_Au\_40% in AAO is shifted to higher values as compared to PE in AAO and PE\_Au\_10% in AAO. This shift, which is far less pronounced than that of  $T_{m,\text{onset}}$ , might be related to the formation of thicker lamellae in PE\_Au\_40% in AAO at higher  $T_c$ .

Overall, these observations corroborate the notion that pronounced homogeneous nucleation at high supercooling contributes to the crystallization of PE and PE\_Au\_10% in AAO, whereas for PE\_Au\_40% in AAO a significant shift to heterogeneous nucleation and growth-dominated crystallization at lower supercooling occurred.

**Crystallization Kinetics and Crystal Orientation.** Shin et al. reported that crystallization of PE confined to AAO resulted in the occurrence of intensity maxima at an azimuthal angle of  $\sim 32^\circ$  with respect to the AAO nanopore axes on the Debye rings belonging to the (110) reflection and concluded that the *b*-axis of orthorhombic PE (or the [020] direction, respectively) is preferentially aligned with the AAO nanopore axes.<sup>4</sup> As discussed above,  $\Theta/2\Theta$  scans (Figure 4) and Schulz scans (Figure 5) of PE, PE\_Au\_10%, and PE\_Au\_40% nonisothermally crystallized in AAO while in contact with a bulk surface reservoir revealed pronounced and uniform alignment of the [020] direction of orthorhombic PE with the AAO nanopore axes. Even crystallization of PE, PE\_Au\_10%, and PE\_Au\_40% in AAO without bulk surface reservoir resulted in prevailing alignment of the [020] direction with the AAO nanopore axes (Figures 6 and 7). We speculate that this outcome can be rationalized as follows. PE crystals formed in a bulk surface reservoir may slowly grow into the AAO nanopores. In the case of PE\_Au\_40% in AAO, PE crystals having any orientation may nucleate at larger Au crystals formed by Ostwald ripening so that heterogeneous nucleation prevails even in the absence of a bulk surface reservoir. At the surfaces of the PE parent crystals thus formed, topographic features may accidentally emerge that can cause nucleation of secondary crystals having their (020) faces

oriented normal to the AAO nanopore axes (Figure 10a). The association of PE chain segments onto (020) faces of PE is

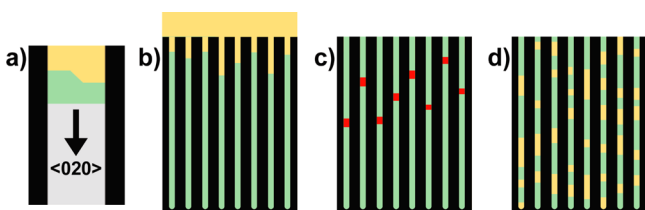


**Figure 10.** Schematic diagram of the proposed mechanism of oriented crystallization (black, AAO pore walls; gray, liquid PE; green, PE crystals having their (020) faces oriented normal to the AAO nanopore axes; orange, PE crystals with other orientations; red, Au crystals formed by Ostwald ripening from AuNPs acting as nucleation sites and/or slowly growing PE crystals nucleated at Au crystals). (a) At low supercooling (high  $T_c$ ), crystallization is dominated by crystal growth and homogeneous nucleation is rare. Secondary nucleation at pre-existing, randomly oriented PE parent crystals formed by heterogeneous nucleation may lead to the formation of PE nuclei having their (020) faces oriented normal to the AAO nanopore axes. Once formed at PE parent crystals originating (b) from bulk PE surface reservoirs or (c) from primary nucleation at Au crystals, secondary PE crystals having their (020) faces oriented normal to the AAO nanopore axes rapidly grow along the AAO nanopores without impinging on competing crystals. (d) In the absence of bulk PE surface reservoirs or Au crystals, crystallization is shifted to lower  $T_c$ s and initiated by formation of many homogeneous nuclei growing into crystals with different orientations.

energetically highly favorable so that the fastest growth of PE crystals occurs along the  $b$ -axis.<sup>18</sup> We assume that the macroscopically strongly preferred alignment of the [020] direction of PE with the AAO nanopore axes has two reasons.

- (1) Under bulk conditions, crystal faces perpendicular to directions associated with high growth rates are commonly short-lived as they grow into edges or vertices.<sup>14,15,42</sup> Hence, the surface of bulk PE crystals typically consists of (110) and (200) faces, whereas (020) faces are not exposed.<sup>18</sup> However, the hard confinement imposed by the rigid walls of the cylindrical AAO nanopores kinetically stabilizes (020) crystal faces oriented perpendicular to the AAO nanopore axes and suppresses formation of crystal faces having dominant morphological importance under bulk conditions.
- (2) The Gibbs free energy of a critical homogeneous nucleus is inversely proportional to the square of supercooling. Therefore, at low supercooling (or high  $T_c$ ) homogeneous nucleation is suppressed. However, the presence of a nucleating surface reduces the free energy barrier for the formation of stable crystalline nuclei. If nucleation can take place on the surfaces of parent PE crystals or sufficiently large gold crystals, these surfaces catalyze nucleation at low supercooling, whereas homogeneous nuclei would only form at higher supercooling. The number of growing crystals at low supercooling is, therefore, limited by the number of heterogeneous nucleation sites. If crystallization is initiated in a PE surface reservoir, only one nucleating surface per AAO nanopore exists: the interface of the (randomly oriented) PE crystal slowly proceeding into the AAO nanopore. As soon as secondary nucleation yields a secondary crystal having its [020] direction aligned with the AAO

nanopore axis, this secondary crystal will rapidly grow along the AAO nanopore without being obstructed by competing crystals (Figure 10b). In the case of PE\_Au\_40% in AAO without a bulk surface reservoir, Au crystals inside the AAO nanopores provide heterogeneous nucleation sites for primary nucleation of slowly growing crystals, from which rapidly growing secondary crystals having their [020] directions aligned with the AAO nanopores may emerge (Figure 10c). Therefore, crystals having their main growth direction, in the case of PE the [020] direction, aligned with the AAO nanopore axes will fill most of the volume of the AAO nanopores, if only a small number of growing crystals generated by heterogeneous nucleation at low supercooling exist.

Nonisothermal crystallization of PE and PE\_Au\_10% in AAO without bulk surface reservoir yielded not only a prevailing subpopulation of crystals having the (020) faces oriented normal to the AAO nanopore axes but also subpopulations of crystals with other orientations. This finding can be rationalized by assuming significant contributions of homogeneous nucleation at higher supercooling. Homogeneous nucleation is an intrinsic material property, and many homogeneous nuclei form within a relatively narrow temperature window. Hence, growth of many competing crystals is initiated. Crystals growing rapidly along the AAO nanopores will have only short free growth paths until they impinge on competing crystals. As a result, crystals with other orientations also have a chance to occupy a certain volume portion of the AAO nanopores (Figure 10d). Then, the dominance of crystallites having (020) faces oriented normal to the AAO nanopore axes is, to some extent, suppressed. However, in the case of PE\_Au\_40% in AAO, crystallization without bulk surface reservoir yielded pronounced and nearly uniform alignment of the [020] direction with the AAO nanopore axes. This outcome suggests in agreement with the results obtained by thermal analysis that the presence of Au crystals promotes heterogeneous nucleation and crystallization dominated by the growth of properly oriented PE crystals at relatively low supercooling.

**Surface Undulations of Released PE\_Au\_40% Nanorods.** We speculate that the surface undulations of released PE\_Au\_40% nanorods seen in Figure 1c may have the following origin. Crystallization arrests amorphous PE chain segments located between the PE lamellae and the AAO pore walls at a state corresponding to  $T_c$  even after cooling to room temperature. Thus, a low-density PE interphase may be preserved as long as the hard confinement imposed by the AAO nanopores persists. Release from AAO replaces the rigid confining AAO nanopore walls by deformable PE/air interfaces. Thus, the amorphous PE chain segments forming the outermost surface of the released PE\_Au\_40% nanorods can relax. As a result, an aged amorphous surface layer surrounding the PE lamellae should form that has a higher density than the PE interphase inside the AAO nanopores. The amorphous PE surface layer of released PE\_Au\_40% nanorods may develop undulations to minimize the surface area. Similar observations were previously reported for block copolymer nanorods subjected to swelling-induced morphology reconstruction.<sup>43</sup>

## CONCLUSION

We have studied the influence of dodecanethiol-capped AuNPs on the melt crystallization of PE in the rigid cylindrical confinement of AAO nanopores. Bulk PE in the presence of 10 or 40 wt % Au showed essentially the same crystallization kinetics than pure bulk PE. Isolated entities of pure PE and PE containing 10 wt % Au inside AAO nanopores exhibited largely undistinguishable crystallization kinetics; crystallization and melting temperatures were shifted to lower values as compared to the corresponding bulk systems, suggesting significant contributions of homogeneous nucleation at large supercooling. However, crystallization of isolated PE entities containing 40 wt % Au in AAO was characterized by a clear shift to heterogeneous nucleation at low supercooling and growth-dominated crystallization. These striking changes attributed to the presence of larger Au crystals acting as heterogeneous nuclei were apparent from the following results. (i) Crystallization temperatures in nonisothermal and isothermal crystallization experiments were shifted to significantly higher values. (ii) Melting temperatures systematically shifted to higher values, indicating formation of more stable PE crystals. (iii) The dependence of crystallization half-times on crystallization temperatures was significantly weaker than for pure PE.

The prevailing alignment of the [020] direction of orthorhombic PE with the AAO nanopore axes was rationalized by the following qualitative model. Crystals having the direction with the highest growth rate oriented along the AAO nanopore axes may form accidentally by secondary nucleation on pre-existing crystal surfaces. The “rough” faces normal to the direction of fastest growth, which vanish under bulk conditions, are kinetically stabilized by the confinement of the rigid AAO nanopore walls. Thus, crystals having their fastest growth direction aligned with the AAO nanopore axes rapidly grow along the AAO nanopores as long as they do not impinge on competing crystals. Uniform alignment of the fastest growing crystal direction with the AAO nanopore axes on a macroscopic scale can be achieved if crystallization is growth-dominated (presence of only a small number of growing crystals), as it is the case if a few heterogeneous nuclei initiate crystallization at low supercooling. The results presented here may contribute to the development of principles for rational mesoscopic crystal engineering in low-dimensional systems. Thus, one-dimensional polymer nanocomposites might be accessible, which have, up to now, largely remained unexplored as functional materials.

## ASSOCIATED CONTENT

### Supporting Information

Figures S1–S5. This material is available free of charge via the Internet at <http://pubs.acs.org>.

## AUTHOR INFORMATION

### Corresponding Author

\*E-mail martin.steinhardt@uos.de.

### Notes

The authors declare no competing financial interest.

## ACKNOWLEDGMENTS

The authors thank Claudia Hess and Heinrich Tobergte for the preparation of AAO as well as the German Research Foundation (STE 1127/13 and INST 190/134-1) and

CICYT MAT2011-24797 for funding. J. Maiz acknowledges support from FPI BES 2009-026632.

## REFERENCES

- (1) Martín, J.; Maiz, J.; Sacristan, J.; Mijangos, C. *Polymer* **2012**, *53*, 1149–1166.
- (2) Steinhart, M.; Senz, S.; Wehrspohn, R. B.; Gösele, U.; Wendorff, J. H. *Macromolecules* **2003**, *36*, 3646–3651.
- (3) Hu, Z.; Baralia, G.; Bayot, V.; Gohy, J. F.; Jonas, A. M. *Nano Lett.* **2005**, *5*, 1738–1743.
- (4) Shin, K.; Woo, E.; Jeong, Y. G.; Kim, C.; Huh, J.; Kim, K. W. *Macromolecules* **2007**, *40*, 6617–6623.
- (5) Wu, H.; Wang, W.; Yang, H.; Su, Z. *Macromolecules* **2007**, *40*, 4244–4249.
- (6) Maiz, J.; Martin, J.; Mijangos, C. *Langmuir* **2012**, *28*, 12296–12303.
- (7) Martín, J.; Mijangos, C.; Sanz, A.; Ezquerra, T. A.; Nogales, A. *Macromolecules* **2009**, *42*, 5395–5401.
- (8) Duran, H.; Steinhart, M.; Butt, H.-J.; Floudas, G. *Nano Lett.* **2011**, *11*, 1671–1675.
- (9) Woo, E.; Huh, J.; Jeong, Y. G.; Shin, K. *Phys. Rev. Lett.* **2007**, *98*, 136103.
- (10) Lutkenhaus, J. L.; McEnnis, K.; Serghei, A.; Russell, T. P. *Macromolecules* **2010**, *43*, 3844–3850.
- (11) Steinhart, M.; Göring, P.; Dernaika, H.; Prabhukaran, M.; Gösele, U.; Hempel, E.; Thurn-Albrecht, T. *Phys. Rev. Lett.* **2006**, *97*, 027801.
- (12) Henschel, A.; Hofmann, T.; Huber, P.; Knorr, K. *Phys. Rev. E* **2007**, *75*, 021607.
- (13) Huang, P.; Zhu, L.; Cheng, S. Z. D.; Ge, Q.; Quirk, R. P.; Thomas, E. L.; Lotz, B.; Hsiao, B. S.; Liu, L.; Yeh, F. *Macromolecules* **2001**, *34*, 6649–6657.
- (14) Bennema, P.; Meekes, H.; Boerrigter, S. X. M.; Cuppen, H. M.; Deij, M. A.; Van Eupen, J.; Verwer, P.; Vlieg, E. *Cryst. Growth Des.* **2004**, *4*, 905–913.
- (15) Lovette, M. A.; Browning, A. R.; Griffin, D. W.; Sizemore, J. P.; Snyder, R. C.; Doherty, M. F. *Ind. Eng. Chem. Res.* **2008**, *47*, 9812–9833.
- (16) Turnbull, D. *J. Chem. Phys.* **1950**, *18*, 198–203.
- (17) Masuda, H.; Fukuda, K. *Science* **1995**, *268*, 1466–1468.
- (18) Keith, H. D. *Polymer* **2003**, *44*, 703–710.
- (19) Hoffman, J. D.; Miller, R. L. *Polymer* **1997**, *38*, 3151–3212.
- (20) Hoffman, J. D.; Froehl, L. J.; Ross, G. S.; Lauritzen, J. I., Jr. *J. Res. Natl. Bur. Stand., Sect. A* **1975**, *79*, 671–699.
- (21) Loo, Y. L.; Register, R. A.; Ryan, A. J. *Phys. Rev. Lett.* **2000**, *84* (18), 4120–4123.
- (22) Loo, Y. L.; Register, R. A.; Ryan, A. J.; Dee, G. T. *Macromolecules* **2001**, *34* (26), 8968–8977.
- (23) Loo, Y. L.; Register, R. A.; Ryan, A. J. *Macromolecules* **2002**, *35* (6), 2365–2374.
- (24) Huang, X.; Ke, Q.; Kim, C.; Zhong, H.; Wei, P.; Wang, G.; Liu, F.; Jiang, P. *Polym. Eng. Sci.* **2007**, *47*, 1052–1061.
- (25) Chen, X.; Shi, J.; Wang, L.; Shi, H.; Liu, Y.; Wang, L. *Polym. Compos.* **2011**, *32*, 177–184.
- (26) Liang, G. D.; Liu, T. T.; Qin, W. P.; Zhu, F. M.; Wu, Q. *Polym. Eng. Sci.* **2012**, *52*, 1250–1257.
- (27) Liang, G. D.; Qin, W. P.; Liu, T. T.; Zhu, F. M.; Wu, Q. *J. Appl. Polym. Sci.* **2012**, *125*, E113–E121.
- (28) Jancar, J.; Fiore, K. *Polymer* **2011**, *52*, 5851–5857.
- (29) Gittins, D. I.; Caruso, F. *Angew. Chem., Int. Ed.* **2001**, *40*, 3001–3004.
- (30) Brust, M.; Walker, M.; Bethell, D.; Schiffrin, D. J.; Whyman, R. J. *Chem. Soc., Chem. Commun.* **1994**, 801–802.
- (31) Cunnane, V. J.; Schiffrin, D. J.; Beltran, C.; Geblewicz, G.; Solomon, T. *J. Electroanal. Chem.* **1988**, *247*, 203–214.
- (32) Scherrer, P. *Nachr. Ges. Wiss. Göttingen Math.-Phys. Klasse* **1918**, *26*, 98–100.
- (33) Schulz, L. G. *J. Appl. Phys.* **1949**, *20*, 1030–1033.

- (34) Steinhart, M.; Zimmermann, S.; Göring, P.; Schaper, A. K.; Gösele, U.; Weder, C.; Wendorff, J. H. *Nano Lett.* **2005**, *5*, 429–434.
- (35) Chernock, W. P.; Beck, P. A. *J. Appl. Phys.* **1952**, *23*, 341–345.
- (36) Hermans, J. J.; Hermans, P. H.; Vermaas, D.; Weidinger, A. *Recl. Trav. Chim. Pays-Bas* **1946**, *65*, 427–447.
- (37) Ostwald, W. *Z. Phys. Chem.* **1900**, *34*, 495–503.
- (38) Göring, P.; Pippel, E.; Hofmeister, H.; Wehrspohn, R. B.; Steinhart, M.; Gösele, U. *Nano Lett.* **2004**, *4*, 1121–1125.
- (39) Butler, M. F.; Donald, A. M.; Bras, W.; Mant, G. R.; Derbyshire, G. E.; Ryan, A. J. *Macromolecules* **1995**, *28*, 6383–6393.
- (40) PDF entry 00-053-1859.
- (41) Avrami, M. *J. Chem. Phys.* **1939**, *7*, 1103–1112.
- (42) Zhang, Y.; Sizemore, J. P.; Doherty, M. F. *AIChE J.* **2006**, *52*, 1906–1915.
- (43) Wang, Y.; Tong, L.; Steinhart, M. *ACS Nano* **2011**, *5*, 1928–1938.